

Heralded entanglement between solid-state qubits separated by three metres

H. Bernien¹, B. Hensen¹, W. Pfaff¹, G. Koolstra¹, M. S. Blok¹, L. Robledo¹, T. H. Taminiau¹, M. Markham², D. J. Twitchen², L. Childress³ & R. Hanson¹

Quantum entanglement between spatially separated objects is one of the most intriguing phenomena in physics. The outcomes of independent measurements on entangled objects show correlations that cannot be explained by classical physics. As well as being of fundamental interest, entanglement is a unique resource for quantum information processing and communication. Entangled quantum bits (qubits) can be used to share private information or implement quantum logical gates^{1,2}. Such capabilities are particularly useful when the entangled qubits are spatially separated^{3–5}, providing the opportunity to create highly connected quantum networks⁶ or extend quantum cryptography to long distances^{7,8}. Here we report entanglement of two electron spin qubits in diamond with a spatial separation of three metres. We establish this entanglement using a robust protocol based on creation of spin-photon entanglement at each location and a subsequent joint measurement of the photons. Detection of the photons heralds the projection of the spin qubits onto an entangled state. We verify the resulting non-local quantum correlations by performing single-shot readout⁹ on the qubits in different bases. The long-distance entanglement reported here can be combined with recently achieved initialization, readout and entanglement operations^{9–13} on local long-lived nuclear spin registers, paving the way for deterministic long-distance teleportation, quantum repeaters and extended quantum networks.

A quantum network can be constructed by using entanglement to connect local processing nodes, each containing a register of well-controlled and long-lived qubits⁶. Solids are an attractive platform for such registers, as the use of nanofabrication and material design may enable well-controlled and scalable qubit systems¹⁴. The potential impact of quantum networks on science and technology has recently spurred research efforts towards generating entangled states of distant solid-state qubits^{15–21}.

A prime candidate for a solid-state quantum register is the nitrogen-vacancy (NV) defect centre in diamond. The NV centre combines a long-lived electronic spin ($S = 1$) with a robust optical interface, enabling measurement and high-fidelity control of the spin qubit^{15,22–24}. Furthermore, the NV electron spin can be used to access and manipulate nearby nuclear spins^{9–13,25}, thereby forming a multi-qubit register. To use such registers in a quantum network requires a mechanism to coherently connect remote NV centres.

Here we demonstrate the generation of entanglement between NV centre spin qubits in distant set-ups. We achieve this by combining recently established spin initialization and single-shot readout techniques⁹ with efficient resonant optical detection and feedback-based control over the optical transitions, all in a single experiment and executed with high fidelity. These results put solid-state qubits on a par with trapped atomic qubits^{3–5} as highly promising candidates for implementing quantum networks.

Our experiment makes use of two NV spin qubits located in independent low-temperature set-ups separated by 3 m (Fig. 1a). We

encode the qubit basis states $|\uparrow\rangle$ and $|\downarrow\rangle$ in the NV spin sublevels $m_S = 0$ and $m_S = -1$, respectively. Each qubit can be independently read out by detecting spin-dependent fluorescence in the NV phonon sideband (non-resonant detection)⁹. The qubits are individually controlled with microwave pulses applied to on-chip striplines²³. Quantum states encoded in the qubits are extremely long-lived: using dynamical decoupling techniques²³, we obtain a coherence time exceeding 10 ms (Fig. 1b), which is the longest coherence time measured so far for a single electron spin in a solid.

We generate and herald entanglement between these distant qubits by detecting the resonance fluorescence of the NV centres. The specific entanglement protocol we use is based on the proposal of ref. 26, and is schematically drawn in Fig. 1c. Both centres NV A and NV B are initially prepared in a superposition $1/\sqrt{2}(|\uparrow\rangle + |\downarrow\rangle)$. Next, each NV centre is excited by a short laser pulse that is resonant with the $|\uparrow\rangle$ to $|e\rangle$ transition, where $|e\rangle$ is an optically excited state with the same spin projection as $|\uparrow\rangle$. Spontaneous emission locally entangles the qubit and photon number, leaving each set-up in the state $1/\sqrt{2}(|\uparrow 1\rangle + |\downarrow 0\rangle)$, where 1 (0) denotes the presence (absence) of an emitted photon; the joint qubit-photon state of both set-ups is then described by $1/2(|\uparrow_A \uparrow_B\rangle|1_A 1_B\rangle + |\downarrow_A \downarrow_B\rangle|0_A 0_B\rangle + |\uparrow_A \downarrow_B\rangle|1_A 0_B\rangle + |\downarrow_A \uparrow_B\rangle|0_A 1_B\rangle)$. The two photon modes, A and B, are directed to the input ports of a beamsplitter (see Fig. 1a), so that fluorescence observed in an output port could have originated from either NV centre. If the photons emitted by the two NV centres are indistinguishable, detection of precisely one photon on an output port would correspond to measuring the photon state $1/\sqrt{2}(|1_A 0_B\rangle \pm e^{-i\varphi}|0_A 1_B\rangle)$ (where φ is a phase that depends on the optical path length). Such a detection event would thereby project the qubits onto the maximally entangled state $|\psi\rangle = 1/\sqrt{2}(|\uparrow_A \downarrow_B\rangle \pm e^{-i\varphi}|\downarrow_A \uparrow_B\rangle)$.

Any realistic experiment, however, suffers from photon loss and imperfect detector efficiency; detection of a single photon is thus also consistent with creation of the state $|\uparrow\uparrow\rangle$. To eliminate this possibility, both qubits are flipped and optically excited for a second time. Because $|\uparrow\uparrow\rangle$ is flipped to $|\downarrow\downarrow\rangle$, no photons are emitted in the second round for this state. In contrast, the states $|\psi\rangle$ will again yield a single photon. Detection of a photon in both rounds thus heralds the generation of an entangled state. The second round not only renders the protocol robust against photon loss, but it also changes φ into a global phase, making the protocol insensitive to the optical path length difference²⁶ (see Supplementary Information). Furthermore, flipping the qubits provides a refocusing mechanism that counteracts spin dephasing during entanglement generation. The final state is one of two Bell states $|\Psi^\pm\rangle = 1/\sqrt{2}(|\uparrow_A \downarrow_B\rangle \pm |\downarrow_A \uparrow_B\rangle)$, with the sign depending on whether the same detector (+) or different detectors (−) clicked in the two rounds.

A key challenge for generating remote entanglement with solid-state qubits is obtaining a large flux of indistinguishable photons, in part because local strain in the host lattice can induce large variations in photon frequency. The optical excitation spectra of the NV centres

¹Kavli Institute of Nanoscience Delft, Delft University of Technology, PO Box 5046, 2600 GA Delft, The Netherlands. ²Element Six Ltd, Kings Ride Park, Ascot, Berkshire SL5 8BP, UK. ³McGill University Department of Physics, 3600 Rue University, Montreal, Quebec H3A 2T8, Canada.

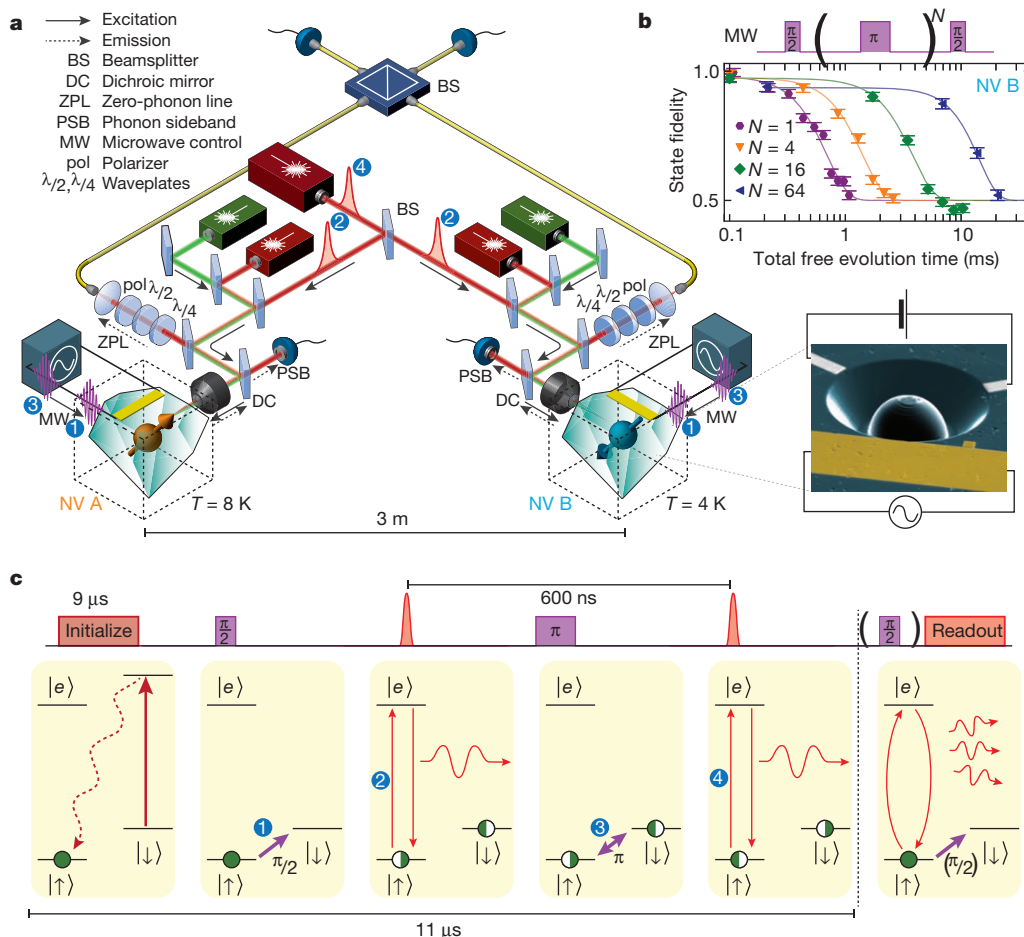


Figure 1 | Experimental set-up and protocol for generating long-distance entanglement between two solid-state spin qubits. **a**, Experimental set-up. Each nitrogen–vacancy (NV) centre resides in a synthetic ultrapure diamond oriented in the $<111>$ direction. The two diamonds are located in two independent low-temperature confocal microscope set-ups separated by 3 m. The NV centres can be individually excited resonantly by red lasers and off-resonantly by a green laser. The emission (dashed arrows) is spectrally separated into an off-resonant part (phonon sideband, PSB) and a resonant part (zero-phonon line, ZPL). The PSB emission is used for independent single-shot readout of the spin qubits⁹. The ZPL photons from the two NV centres are overlapped on a fibre-coupled beamsplitter. Microwave pulses for spin control are applied via on-chip microwave striplines. An applied magnetic field of 17.5 G splits the $m_s = \pm 1$ levels in energy. The optical frequencies of NV B are tuned by a d.c. electric field applied to the gate electrodes (inset, scanning

(Fig. 2a) display sharp spin-selective transitions. Here we use the E_y transition (spin projection $m_s = 0$) in the entangling protocol and for qubit readout; we use the A_1 transition for fast optical pumping into $| \uparrow \rangle$ (ref. 9). Owing to different strain in the two diamonds, the frequencies of the E_y transitions differ by 3.5 GHz, more than 100 linewidths. By applying a voltage to an on-chip electrode (Fig. 1a inset), we tune the optical transition frequencies of one centre (NV B) through the d.c. Stark effect^{18,27} and bring the E_y transitions of the two NV centres into resonance (Fig. 2a bottom).

Charge fluctuations near the NV centre also affect the optical frequencies. To counteract photo-ionization, we need to regularly apply a green laser pulse to repump the NV centre into the desired charge state. This repump pulse changes the local electrostatic environment, leading to jumps of several linewidths in the optical transition frequencies²⁸. To overcome these effects, we only initiate an experiment if the number of photons collected during a two-laser probe stage (Fig. 2b) exceeds a threshold, thereby ensuring that the NV centre's optical transitions are on resonance with the lasers. The preparation procedure markedly

electron microscope image of a similar device). To enhance the collection efficiency, solid immersion lenses have been milled around the two NV centres⁹. **b**, The coherence of the NV B spin qubit as a function of total free evolution time t_{FE} during an N -pulse dynamical decoupling sequence²³. Curves are fitted to $A \exp[-(t_{\text{FE}}/T_{\text{coh}})^3] + 0.5$. For $N = 64$ we find $T_{\text{coh}} = 14.3 \pm 0.4$ ms. Error bars are 2 s.e. **c**, Entanglement protocol (details in main text), illustrating the pulse sequence applied simultaneously to both NV centres. Both NV centres are initially prepared in a superposition $1/\sqrt{2}(| \uparrow \rangle + | \downarrow \rangle)$. A short 2 ns spin-selective resonant laser pulse creates spin-photon entanglement $1/\sqrt{2}(| \uparrow \rangle + | \downarrow \rangle)$. The photons are overlapped on the beamsplitter and detected in the two output ports. Both spins are then flipped, and the NV centres are excited a second time. The detection of one photon in each excitation round heralds the entanglement and triggers individual spin readout.

improves the observed optical coherence: as the probe threshold is increased, optical Rabi oscillations persist for longer times (see Fig. 2b). For high thresholds, the optical damping time saturates around the value expected for a lifetime-limited linewidth²⁸, indicating that the effect of spectral jumps induced by the repump laser is strongly mitigated.

Besides photon indistinguishability, successful execution of the protocol also requires that the detection probability of resonantly emitted photons exceed that of scattered laser photons and of detector dark counts. This is particularly demanding for NV centres, because only about 3% of their emission is in the zero-phonon line and useful for the protocol. To minimize detection of laser photons, we use both a cross-polarized excitation–detection scheme (Fig. 2c inset) and a detection time filter that exploits the difference between the length of the laser pulse (2 ns) and the NV centre's excited-state lifetime (12 ns; Fig. 2c). For a typical detection window used, this reduces the contribution of scattered laser photons to about 1%. Combined with microfabricated solid-immersion lenses for enhanced collection efficiency (Fig. 1a

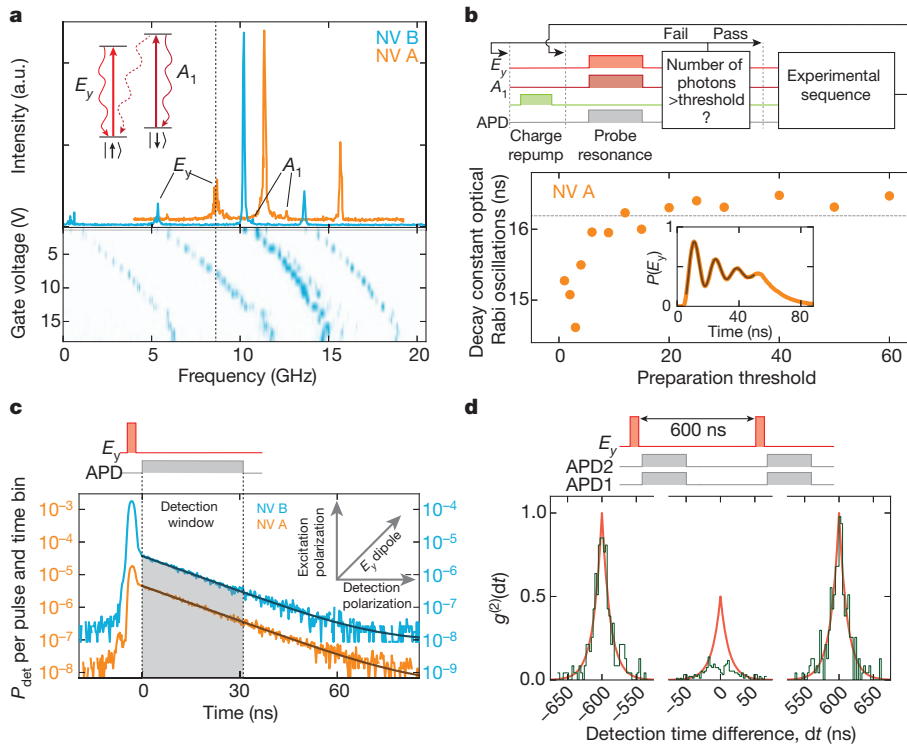


Figure 2 | Generating and detecting indistinguishable photons.

a, Photoluminescence excitation spectra of NV A and NV B; frequency is given relative to 470.4515 THz. Transitions are labelled according to the symmetry of their excited state. The A_1 transition is used to initialize the NV centre into the $|\uparrow\rangle$ state ($m_s = 0$) and the E_y transition is used for entanglement creation and single-shot readout. By applying a voltage to the gate electrodes of NV B, the E_y transitions are tuned into resonance (dashed line). **b**, Dynamical preparation of charge and optical resonance. Top, preparation protocol. A 10 μ s green laser pulse (green line) pumps the NV centre into the desired negative charge state⁹. Next, the optical transition frequencies are probed by simultaneously exciting the E_y and A_1 transitions for 60 μ s while counting the number of detected photons. Conditional on passing a certain threshold the experimental sequence is started (preparation successful) or else the protocol is repeated (preparation failed). APD, avalanche photodiode. Bottom, line-narrowing effect of the preparation protocol exemplified by the dependence of the decay time of

optical Rabi oscillations on preparation threshold. Dashed line indicates lifetime-limited damping²⁸. For the entanglement experiment, we choose a threshold of 45 (20) photons for NV A (NV B). **c**, Resonant optical excitation and detection. The polarization axis of the detection path is aligned perpendicular to the excitation axis. The dipole axis of the E_y transition is oriented in between these two axes (inset). Remaining laser light reflection is time-filtered by defining a photon detection window that starts after the laser pulse. Data are recorded with 256 ps time bins. P_{det} , detection probability.

d, Two-photon quantum interference using resonant excitation and detection. The $g^{(2)}$ correlation function is obtained from all coincidence detection events of APD 1 and APD 2 during the entanglement experiment (see Supplementary Information). The sidepeaks are fitted to an exponential decay; from the fit values, we obtain the expected central peak shape $g_{\perp}^{(2)}$ (red line) for non-interfering photons. The visibility of the interference is given by $(g_{\perp}^{(2)} - g_{\parallel}^{(2)})/g_{\perp}^{(2)}$.

inset) and spectral filtering for suppressing non-resonant NV emission, we obtain a detection probability of a resonant NV photon of about 4×10^{-4} per pulse—about 70 times higher than the sum of background contributions.

The degree of photon indistinguishability and background suppression can be obtained directly from the second-order autocorrelation function $g^{(2)}$, which we extract from our entanglement experiment (see Supplementary Information). For fully distinguishable photons, the value of $g^{(2)}$ would reach 0.5 at zero arrival time difference. A strong deviation from this behaviour is observed (Fig. 2d) due to two-photon quantum interference²⁹ that, for perfectly indistinguishable photons, would make the central peak fully vanish. The remaining coincidences are likely to be caused by (temperature-dependent) phonon-induced transitions between optically excited states³⁰ in NV A (these transitions are less relevant for NV B because it is at a lower temperature). The visibility of the two-photon interference observed here— $(80 \pm 5)\%$ for $|dt| < 2.56$ ns—is a significant improvement over previously measured values^{18,19} and central to the success of the entangling scheme.

To generate and detect remote entanglement experimentally, we run the following sequence: first, both NV centres are independently prepared into the correct charge state and brought into optical resonance according to the scheme in Fig. 2b. Then we apply the entangling protocol shown in Fig. 1c using a 600 ns delay between the two optical excitation rounds. We repeat the protocol 300 times before we

return to the resonance preparation step; this number is a compromise between maximizing the attempt rate and minimizing the probability of NV centre ionization. A fast logic circuit monitors the photon counts in real time and triggers single-shot qubit readout on each set-up whenever entanglement is heralded, that is, whenever a single photon is detected in each round of the protocol. The readout projects each qubit onto the $|\{\uparrow\}, |\downarrow\}\rangle$ states (Z -basis), or onto the $|\{\uparrow\pm|\downarrow\}, |\uparrow\mp|\downarrow\}\rangle$ states (X or $-X$ basis). The latter two are achieved by first rotating the qubit by $\pi/2$ using a microwave pulse before readout. By correlating the resulting single-qubit readout outcomes, we can verify the generation of the desired entangled states. To obtain reliable estimates of the two-qubit state probabilities, we correct the raw data with a maximum-likelihood method for local readout errors. These readout errors are known accurately from regular calibrations performed during the experiment (see Supplementary Information).

Figure 3 shows the obtained correlations. When both qubits are measured along Z (readout basis $\{Z, Z\}$), the states Ψ^+ and Ψ^- (as identified by their different photon signatures) display strongly anti-correlated readout results (odd parity). The coherence of the joint qubit state is revealed by measurements performed in rotated bases ($\{X, X\}$, $\{-X, X\}$), which also exhibit significant correlations. Furthermore, these measurements allow us to distinguish between states Ψ^+ and Ψ^- . For Ψ^+ the $\{X, X\}$ ($\{-X, X\}$) outcomes exhibit even (odd) parity, whereas the Ψ^- state displays the opposite behaviour, as expected. The

observed parities demonstrate that the experiment yields the two desired entangled states.

We calculate a strict lower bound on the state fidelity by combining the measurement results from different bases (see Supplementary Information):

$$F = \langle \Psi^\pm | \rho | \Psi^\pm \rangle \geq 1/2(P_{\uparrow\downarrow} + P_{\downarrow\uparrow} + C) - \sqrt{(P_{\uparrow\downarrow}P_{\downarrow\uparrow})} \quad (1)$$

where P_{ij} is the probability for the measurement outcome ij in the $\{Z, Z\}$ basis (that is, the diagonal elements of the density matrix ρ) and C is the contrast between odd and even outcomes in the rotated bases. We find a lower bound of $(69 \pm 5)\%$ for Ψ^- and $(58 \pm 6)\%$ for Ψ^+ , and probabilities of 99.98% and 91.8% , respectively, that the state fidelity is above the classical limit of 0.5 . These values firmly establish that we have created remote entanglement, and are the main result of this Letter.

The lower bound on the state fidelity given above takes into account the possible presence of coherence within the even-parity subspace $\{\uparrow\uparrow, \downarrow\downarrow\}$. However, the protocol selects out states with odd parity and therefore this coherence is expected to be absent (see Supplementary Information). To compare the results to the expected value and to account for sources of error, we set the related (square-root) term in equation (1) to zero and obtain for the data in Fig. 3 as best estimate $F = (73 \pm 4)\%$ for Ψ^- and $F = (64 \pm 5)\%$ for Ψ^+ .

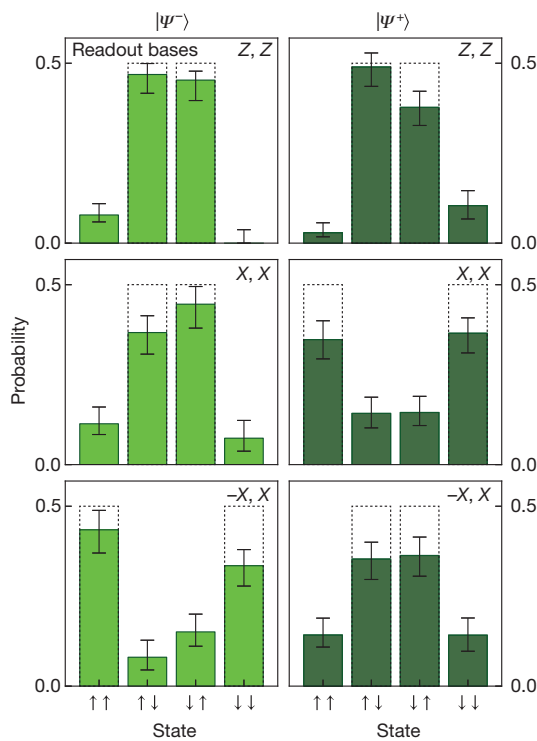


Figure 3 | Verification of entanglement using spin–spin correlations. Each time that entanglement is heralded the spin qubits are individually read out and their results correlated. The readout bases for NV A and NV B can be rotated by individual microwave control (see text). The state probabilities are obtained by a maximum-likelihood estimation on the raw readout results (see Supplementary Information). Error bars depict 68% confidence intervals; dashed lines indicate expected results for perfect state fidelity. Data are obtained from 739 heralding events. For Ψ^- , the detection window in each round is set to 38.4 ns, and the maximum absolute detection time difference $|\delta\tau|$ between the two photons relative to their laser pulses is restricted to 25.6 ns. $\delta\tau = \tau_2 - \tau_1$, where τ_1 is the arrival time of the first photon relative to the first laser pulse and τ_2 the arrival time of the second photon relative to the second laser pulse. For Ψ^+ the second detection window is set to 19.2 ns with $|\delta\tau| < 12.8$ ns, in order to reduce the effect of photo-detector afterpulsing.

Several known error sources contribute to the observed fidelity. Most importantly, imperfect photon indistinguishability reduces the coherence of the state. In Fig. 4a we plot the maximum state fidelity expected from photon interference data (Fig. 2d) together with the measured state fidelities, as a function of the maximum allowed difference in detection time of the two photons relative to their respective laser pulses. We find that the fidelity can be slightly increased by restricting the data to smaller time differences, albeit at the cost of a lower success rate (Fig. 4b).

The fidelity is further decreased by errors in the microwave pulses (estimated at 3.5%), spin initialization (2%), spin decoherence ($<1\%$) and spin flips during the optical excitation (1%) (see Supplementary Information). Moreover, Ψ^+ is affected by afterpulsing, whereby detection of a photon in the first round triggers a fake detector click in the second round. Such afterpulsing leads to a distortion of the correlations (see, for example, the increased probability for $|\downarrow\downarrow\rangle$ in Fig. 3) and thereby a reduction in fidelity for Ψ^+ (see Supplementary Information). Besides these errors that reduce the actual state fidelity, the measured value is also slightly lowered by a conservative estimation for readout errors and by errors in the final microwave $\pi/2$ pulse used for reading out in a rotated basis.

The fidelity of the remote entanglement could be significantly increased in future experiments by further improving photon indistinguishability. This may be achieved by more stringent frequency selection in the resonance initialization step and by working at lower temperatures, which will reduce phonon-mediated excited-state mixing³⁰. Also, the microwave errors can be much reduced; for instance, by using isotopically purified diamonds¹² and polarizing the host nitrogen nuclear spin⁹.

The success probability of the protocol is given by $P_\Psi = 1/2 \eta_A \eta_B$. Here η_i is the overall detection efficiency of resonant photons from NV i and the factor $1/2$ takes into account cases where the two spins are projected into $|\downarrow\downarrow\rangle$ or $|\uparrow\uparrow\rangle$, which are filtered out by their different photon signature. In the current experiment, we estimate $P_\Psi \approx 10^{-7}$ from the data in Fig. 2c. The entanglement attempt rate is about

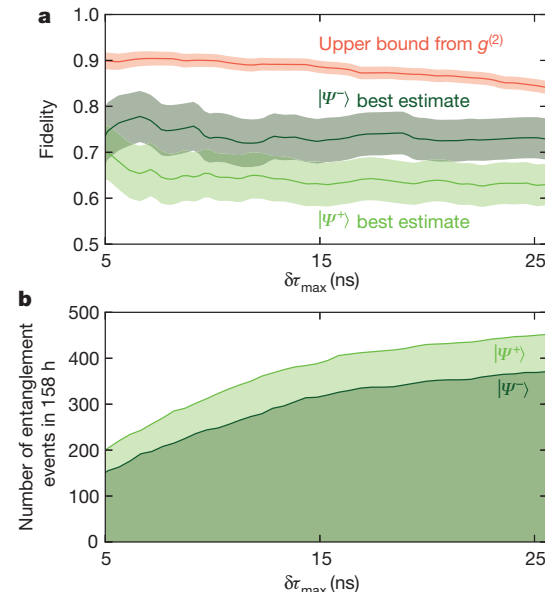


Figure 4 | Dependence of the fidelity and the number of entanglement events on the detection time difference of the photons. **a**, Upper bound on the state fidelity from photon interference data (see Supplementary Information) and best estimate of the state fidelity from the correlation data as a function of the maximum allowed photon detection time difference ($|\delta\tau| < \delta\tau_{\max}$). Detection time windows are chosen as in Fig. 3. Shaded regions indicate 68% confidence intervals. **b**, Number of entanglement events obtained during 158 h as a function of the maximum allowed photon detection time difference, $\delta\tau_{\max}$.

20 kHz, yielding one entanglement event per 10 min. This is in good agreement with the 739 entanglement events obtained over a time of 158 h. The use of optical cavities would greatly enhance both the collection efficiency and emission in the zero-phonon line³¹ and increase the success rate by several orders of magnitude.

Creation of entanglement between distant spin qubits in diamond, as reported here, opens the door to extending the remarkable properties of NV-based quantum registers towards applications in quantum information science. By transferring entanglement to nuclear spins near each NV centre, a non-local state might be preserved for seconds or longer¹², facilitating the construction of cluster states² or quantum repeaters⁸. At the same time, the auxiliary nuclear spin qubits also provide an excellent resource for processing and error correction. When combined with future advances in nanofabricated integrated optics and electronics, the use of electrons and photons as quantum links and nuclear spins for quantum processing and memory offers a compelling route towards realization of solid-state quantum networks.

Received 24 December 2012; accepted 14 February 2013.

Published online 24 April 2013.

1. Nielsen, M. A. & Chuang, I. L. *Quantum Computation and Quantum Information* (Cambridge Univ. Press, 2000).
2. Raussendorf, R. & Briegel, H. J. A. One-way quantum computer. *Phys. Rev. Lett.* **86**, 5188–5191 (2001).
3. Moehring, D. L. *et al.* Entanglement of single-atom quantum bits at a distance. *Nature* **449**, 68–71 (2007).
4. Ritter, S. *et al.* An elementary quantum network of single atoms in optical cavities. *Nature* **484**, 195–200 (2012).
5. Hofmann, J. *et al.* Heralded entanglement between widely separated atoms. *Science* **337**, 72–75 (2012).
6. Kimble, H. J. The quantum internet. *Nature* **453**, 1023–1030 (2008).
7. Duan, L. M., Lukin, M. D., Cirac, J. I. & Zoller, P. Long-distance quantum communication with atomic ensembles and linear optics. *Nature* **414**, 413–418 (2001).
8. Childress, L., Taylor, J. M., Sørensen, A. S. & Lukin, M. D. Fault-tolerant quantum communication based on solid-state photon emitters. *Phys. Rev. Lett.* **96**, 070504 (2006).
9. Robledo, L. *et al.* High-fidelity projective read-out of a solid-state spin quantum register. *Nature* **477**, 574–578 (2011).
10. Neumann, P. *et al.* Single-shot readout of a single nuclear spin. *Science* **329**, 542–544 (2010).
11. Neumann, P. *et al.* Multipartite entanglement among single spins in diamond. *Science* **320**, 1326–1329 (2008).
12. Maurer, P. C. *et al.* Room-temperature quantum bit memory exceeding one second. *Science* **336**, 1283–1286 (2012).
13. Pfaff, W. *et al.* Demonstration of entanglement-by-measurement of solid-state qubits. *Nature Phys.* **9**, 29–33 (2013).
14. Ladd, T. D. *et al.* Quantum computers. *Nature* **464**, 45–53 (2010).
15. Togan, E. *et al.* Quantum entanglement between an optical photon and a solid-state spin qubit. *Nature* **466**, 730–734 (2010).
16. Gao, W. B., Fallahi, P., Togan, E., Miguel-Sánchez, J. & Imamoglu, A. Observation of entanglement between a quantum dot spin and a single photon. *Nature* **491**, 426–430 (2012).
17. De Greve, K. *et al.* Quantum-dot spin-photon entanglement via frequency downconversion to telecom wavelength. *Nature* **491**, 421–425 (2012).
18. Bernien, H. *et al.* Two-photon quantum interference from separate nitrogen vacancy centers in diamond. *Phys. Rev. Lett.* **108**, 043604 (2012).
19. Sipahigil, A. *et al.* Quantum interference of single photons from remote nitrogen-vacancy centers in diamond. *Phys. Rev. Lett.* **108**, 143601 (2012).
20. Patel, R. B. *et al.* Two-photon interference of the emission from electrically tunable remote quantum dots. *Nature Photon.* **4**, 632–635 (2010).
21. Flagg, E. B. *et al.* Interference of single photons from two separate semiconductor quantum dots. *Phys. Rev. Lett.* **104**, 137401 (2010).
22. Fuchs, G. D., Dobrovitski, V. V., Toyli, D. M., Heremans, F. J. & Awschalom, D. D. Gigahertz dynamics of a strongly driven single quantum spin. *Science* **326**, 1520–1522 (2009).
23. De Lange, G., Wang, Z. H., Ristè, D., Dobrovitski, V. V. & Hanson, R. Universal dynamical decoupling of a single solid-state spin from a spin bath. *Science* **330**, 60–63 (2010).
24. van der Sar, T. *et al.* Decoherence-protected quantum gates for a hybrid solid-state spin register. *Nature* **484**, 82–86 (2012).
25. Dolde, F. *et al.* Room-temperature entanglement between single defect spins in diamond. *Nature Phys.* **9**, 139–143 (2013).
26. Barrett, S. D. & Kok, P. Efficient high-fidelity quantum computation using matter qubits and linear optics. *Phys. Rev. A* **71**, 060310 (2005).
27. Bassett, L. C., Heremans, F. J., Yale, C. G., Buckley, B. B. & Awschalom, D. D. Electrical tuning of single nitrogen-vacancy center optical transitions enhanced by photoinduced fields. *Phys. Rev. Lett.* **107**, 266403 (2011).
28. Robledo, L., Bernien, H., Van Weperen, I. & Hanson, R. Control and coherence of the optical transition of single nitrogen vacancy centers in diamond. *Phys. Rev. Lett.* **105**, 177403 (2010).
29. Hong, C. K., Ou, Z. Y. & Mandel, L. Measurement of subpicosecond time intervals between two photons by interference. *Phys. Rev. Lett.* **59**, 2044–2046 (1987).
30. Fu, K.-M. C. *et al.* Observation of the dynamic Jahn-Teller effect in the excited states of nitrogen-vacancy centers in diamond. *Phys. Rev. Lett.* **103**, 256404 (2009).
31. Aharonovich, I., Greentree, A. D. & Prawer, S. Diamond photonics. *Nature Photon.* **5**, 397–405 (2011).

Supplementary Information is available in the online version of the paper.

Acknowledgements We thank F. Jelezko, P. Kok, M. Lukin, J. Morton, E. Togan and L. Vandersypen for discussions and comments, and R.N. Schouten and M.J. Tiggelman for technical assistance. We acknowledge support from the Dutch Organization for Fundamental Research on Matter (FOM), the Netherlands Organization for Scientific Research (NWO), the DARPA QuASAR programme, the EU SOLID, DIAMANT and S3NANO programmes and the European Research Council through a Starting Grant.

Author Contributions H.B., B.H., L.R., L.C. and R.H. designed the experiment. H.B., B.H., W.P., G.K. and M.S.B. performed the experiments. H.B., B.H., W.P., G.K., M.S.B., T.H.T. and R.H. analysed the results. H.B., M.M. and D.J.T. fabricated the devices. H.B., B.H., W.P., M.S.B., L.C. and R.H. wrote the manuscript. All authors discussed the results and commented on the manuscript.

Author Information Reprints and permissions information is available at www.nature.com/reprints. The authors declare no competing financial interests. Readers are welcome to comment on the online version of the paper. Correspondence and requests for materials should be addressed to R.H. (r.hanson@tudelft.nl).